

# Metal—organic framework derived multicomponent nanoagent as a reactive oxygen species amplifier for enhanced photodynamic therapy

Wang, Dongdong; Wu, Huihui; Yang, Guangbao; Qian, Cheng; Gu, Long; Wang, Hou; Zhou, Weiqiang; Liu, Jiawei; Wu, Yinglong; Zhang, Xiaodong; Guo, Zhen; Chen, Hongzhong; Jana, Deblin; Zhao, Yanli

2020

Wang, D., Wu, H., Yang, G., Qian, C., Gu, L., Wang, H., ... Zhao, Y. (2020). Metal—organic framework derived multicomponent nanoagent as a reactive oxygen species amplifier for enhanced photodynamic therapy. *ACS Nano*, 14(10), 13500–13511.  
doi:10.1021/acsnano.0c05499

<https://hdl.handle.net/10356/146323>

<https://doi.org/10.1021/acsnano.0c05499>

---

This document is the Accepted Manuscript version of a Published Work that appeared in final form in *ACS Nano*, copyright © American Chemical Society after peer review and technical editing by the publisher. To access the final edited and published work see <https://doi.org/10.1021/acsnano.0c05499>

*Downloaded on 20 Mar 2024 19:25:58 SGT*

# Metal-Organic Framework Derived Multicomponent Nanoagent as a Reactive Oxygen Species Amplifier for Enhanced Photodynamic Therapy

Dongdong Wang,<sup>†</sup> Huihui Wu,<sup>‡</sup> Guangbao Yang,<sup>†</sup> Cheng Qian,<sup>†</sup> Long Gu,<sup>†</sup> Hou Wang,<sup>†</sup> Weiqiang Zhou,<sup>†</sup> Jiawei Liu,<sup>†</sup> Yinglong Wu,<sup>†</sup> Xiaodong Zhang,<sup>†</sup> Zhen Guo,<sup>‡,\*</sup> Hongzhong Chen,<sup>†</sup> Deblin Jana,<sup>†</sup> Yanli Zhao<sup>†,\*</sup>

<sup>†</sup>Division of Chemistry and Biological Chemistry, School of Physical and Mathematical Sciences, Nanyang Technological University, 21 Nanyang Link, Singapore 637371, Singapore.

<sup>‡</sup>Anhui Key Laboratory for Cellular Dynamics and Chemical Biology, School of Life Sciences, University of Science and Technology of China, Hefei 230027, P. R. China.

**ABSTRACT:** Intracellular antioxidants such as glutathione (GSH) play a critical role in protecting malignant tumor cells from apoptosis induced by reactive oxygen species (ROS) and in mechanisms of multidrug and radiation resistance. Herein, we rationally design two multicomponent self-assembled photodynamic therapy (PDT) nanoagents, *i.e.*, Glup-MFi-c and Glud-MFo-c, which consist of respective GSH-passivation and GSH-depletion linkers in metal-organic frameworks encapsulated with photosensitizers for a deeply comprehensive understanding of GSH-based tumor PDT. Multicomponent coordination,  $\pi$ - $\pi$  stacking, and electrostatic interactions among metal ions, photosensitizers, and bridging linkers under the protection of a biocompatible polymer generate homogeneous nanoparticles with satisfied size, good colloid stability, and ultrahigh loading capacity. Compared to the GSH-passivated Glup-MFi-c, the GSH-depleted Glud-MFo-c shows pH-responsive release of photosensitizer and  $[\text{Fe}^{\text{III}}(\text{CN})_6]$  linker in tumor cells to efficiently deplete intracellular GSH, thus amplifying the cell-killing efficiency of ROS and suppressing the tumor growth *in vivo*. This study demonstrates that Glud-MFo-c acts as a ROS amplifier, providing a useful strategy to deeply understand the role of GSH in combating cancer.

**KEYWORDS:** glutathione; metal-organic frameworks; photodynamic therapy; reactive oxygen species; self-assembly

Photodynamic therapy (PDT) involves non-toxic photosensitizers and localized oxygen to produce cytotoxic reactive oxygen species (ROS) with the administration of harmless excitation light.<sup>1,2</sup> It shows superior advantages as a clinical therapeutic strategy for various superficial and localized cancers or lesions.<sup>3,4</sup> With spatiotemporal control over the localization of light irradiation, PDT could improve the selectivity and minimize side effects compared to common modalities such as surgery, radiotherapy, and chemotherapy.<sup>5-7</sup> As a key element of PDT, low bioavailability, poor tumor selectivity and hydrophobic property of photosensitizers severely compromise its therapeutic efficiency. Thus, one popular strategy is to construct nanosystems for improving the bioavailability and tumor targeting through enhanced permeation retention (EPR) effect.<sup>8,9</sup> Such strategy has been envisioned to improve the PDT outcomes.<sup>10</sup> Cancer cells maintain an altered intracellular redox state, typically featuring high levels of antioxidants, especially glutathione (GSH) with a higher concentration (4~10 folds) than that in normal cells.<sup>11-13</sup> GSH appears to be actively involved in protecting cancer cells from apoptosis and accounts for multidrug and radiation resistance, mainly through scavenging cellular ROS.<sup>14,15</sup> Thus, modulation of intracellular GSH metabolism is a potential approach to affect the efficiency of antitumor therapies, as the elimination of antioxidants would cause rapid accumulation of ROS.<sup>16-18</sup> Previous studies have shown that the combination of GSH-depletion with other treatments such as chemodynamic therapy, sonodynamic therapy, PDT, and immunotherapy can generate synergistic therapeutic efficacy.<sup>18-23</sup> Those GSH-depletion platforms based on inorganic nanoparticles are usually involved with high valence metal ions (such as  $\text{Cu}^{2+}$ ,  $\text{W}^{6+}$ , and  $\text{Mn}^{4+}$ ), showing oxidation-reduction reactions toward intracellular GSH. Nevertheless, sufficient evidence is required to deeply understand the role of GSH-depletion for synergistic therapeutic effect by designing GSH-passivation nanoparticles as a control.

Self-assembled nanoagents integrate the adaptability of supramolecular self-assembly and the simplicity of spatiotemporal control over cargo delivery are promising for personalized, effective, and noninvasive cancer therapy.<sup>24,25</sup> Recently, metal-organic frameworks (MOFs) have attracted considerable research attention in constructing self-assembly systems due to well-defined coordination network and tunable porosity.<sup>26-29</sup> Through rational integration of cargos, metal ions, and organic linkers, functional nanostructures can be fabricated through the interactions among building blocks and cargos.<sup>30,31</sup> Prussian blue analogues (PBAs) are a subclass of MOFs with a nominal composition of  $\text{M}_a[\text{M}_b(\text{CN})_6]$  and show a close parallel to the double-perovskite structure.<sup>32-34</sup>  $\text{Mn}_3[\text{Fe}(\text{CN})_6]_2$  is a typical PBA, in which Mn is octahedrally coordinated to six bridging linkers with N terminals.<sup>35-37</sup> The special Mn-N<sub>6</sub> (S = 5/2) structure with high-spin state in the skeleton endows  $\text{Mn}_3[\text{Fe}(\text{CN})_6]_2$  with excellent magnetic resonance

(MR) imaging ability for *in vivo* tracking of the nanoparticles, Besides, it also shows rapid pH-responsive degradation on account of relatively weak coordination interaction between Mn ion and bridging linkers. Moreover, the  $[\text{Fe}^{\text{III}}(\text{CN})_6]$  linkers with polarizable  $\pi$ -electron cloud also provide  $\pi$ - $\pi$  stacking with  $\pi$ -conjugated cargos. Thus, various cargos could be encapsulated during the one-pot synthesis process. Such one-pot *in situ* encapsulation during the synthesis of MOFs is economic and can avoid the waste of raw materials, realizing the full utilization of building blocks. As far as we know, there is no report deeply exploring the role of GSH-depletion in combating cancer through such multicomponent nanoagents by integrating self-assembly and pH-responsive cargo release into one system.

Herein, we report the use of PBAs as parent materials to realize feasible multicomponent self-assembly in fabricating photodynamic nanoagents for antitumor therapy (Figure 1). Facilitated by the multicomponent coordination interactions, photosensitizers, metal ions, and organic ligands can self-assemble to form well-defined GSH-depletion  $\text{Mn}_3[\text{Fe}(\text{CN})_6]_2\text{-Ce6}$  nanoagent (Glud-MFo-c) under the protection of biocompatible poly-vinylpyrrolidone (PVP) polymer. Within the acidic tumor microenvironment, pH-responsive degradation of nanoagents can trigger the release of Ce6 molecule to generate ROS under light irradiation. The released  $[\text{Fe}^{\text{III}}(\text{CN})_6]$  linkers will further be reduced to  $[\text{Fe}^{\text{II}}(\text{CN})_6]$  linkers through intracellular GSH depletion. In addition,  $T_1$ -weighted MR imaging ability arising from the Mn-N<sub>6</sub> structure endows *in vivo* tracking of the nanoagent. The work presents a self-assembled multicomponent nanoagent that not only integrates imaging and cancer therapy, but also shows zero-waste utilization of all building blocks. The formulation contains materials generally regarded as safe by the U.S. Food and Drug Administration (FDA), which promises a rapid clinical translation. Those results demonstrate the Glud-MFo-c is an effective ROS amplifier for antitumor theranostics.

## RESULTS AND DISCUSSION

**Synthesis of Glud-MFo and Glup-MFi.** In order to deeply understand the role of GSH-depletion for enhanced PDT, we rationally designed two nanoagents, *i.e.*, Glud-MFo-c and Glup-MFi-c, possessing GSH-depletion and GSH-passivation abilities, respectively (Figures 1 and S1). Firstly, two short bridging linkers ferrocyanide  $[\text{Fe}^{\text{III}}(\text{CN})_6]$  and ferricyanide  $[\text{Fe}^{\text{II}}(\text{CN})_6]$  were selected to fabricate two pure MOFs through one-pot *in situ* self-assembly process (Figure S2). Biocompatible nonionic PVP polymer was applied as surfactant, since it is highly water-soluble and shows good stability in living tissues.<sup>38</sup> In addition, previous studies have proven that PVP is a suitable polymeric modifier for prolonging the circulation lifetime



of drugs in blood.<sup>39,40</sup> MOF suspensions were generated upon mixing  $[\text{Fe}^{\text{III}}(\text{CN})_6]$  ( $0.71 \text{ mg mL}^{-1}$ ) or  $[\text{Fe}^{\text{II}}(\text{CN})_6]$  ( $0.71 \text{ mg mL}^{-1}$ ) with Mn ion ( $0.37 \text{ mg mL}^{-1}$  in the formation of  $\text{Mn}(\text{CH}_3\text{COO})_2 \cdot 4\text{H}_2\text{O}$  or  $\text{MnSO}_4 \cdot \text{H}_2\text{O}$ ) in the presence of biocompatible PVP ( $10 \text{ mg/mL}$ ) polymer, suggesting the successful synthesis of GSH-depletion  $\text{Mn}_3[\text{Fe}(\text{CN})_6]_2$  (denoted as Glud-MFo, with a yellow-brown color) or GSH-passivation  $\text{Mn}_2[\text{Fe}(\text{CN})_6]$  (denoted as Glup-MFi, with a white-milk color). As revealed by scanning electron microscopy (SEM) and transmission electron microscopy (TEM), Glud-MFo showed nearly cubic morphology with  $100 \text{ nm}$  in diameter (Figure 2a,b). On account of the similar microstructure of Glup-MFi to that of Glud-MFo, SEM and TEM also witnessed nearly cubic morphology with a diameter of  $100 \text{ nm}$  for Glup-MFi nanoparticles (Figure 2c,d).

Next, we studied the pH-responsive and GSH-depletion abilities of the two MOFs. As shown in Figure 2e, Glud-MFo exhibited rapid degradation when immersed into acidic phosphate-buffered saline (PBS) solution with a pH value of 5.0. This phenomenon is consistent with previous report about Mn-doped Prussian blue nanoparticles.<sup>41</sup> With the following addition of GSH, the color of the solution changed from yellow to transparent, indicating that the  $[\text{Fe}^{\text{III}}(\text{CN})_6]$  linker was reduced to  $[\text{Fe}^{\text{II}}(\text{CN})_6]$  linker by GSH through oxidation-reduction reaction (ORR). Akin to Glud-MFo-c, Glup-MFi also showed a rapid pH-responsive degradation profile (Figure 2f). In contrast, as the building block  $[\text{Fe}^{\text{II}}(\text{CN})_6]$  linkers of Glup-MFi already stays at its reduction state, the color of supernatant did not show any changes with the addition of GSH. As identified by powder X-ray diffraction (XRD) analysis, both Glup-MFi and Glud-MFo showed high crystallinity with typical PBA diffraction peaks, which are consistent with previous reports (Figures 2g and S3).<sup>42</sup> To further confirm the GSH-depletion and GSH-passivation abilities of two MOFs, X-ray photoelectron spectroscopy (XPS) analysis was performed to study the oxidation state of central Fe element. As shown in Figure 2h, Glup-MFi presented the characteristic peaks with binding energies at  $707.5 \text{ eV}$  and  $721.5 \text{ eV}$  in the Fe XPS spectrum, which should be assigned to  $\text{Fe}_{3/2}$  and  $\text{Fe}_{1/2}$  of central  $\text{Fe}^{\text{II}}$  in  $[\text{Fe}^{\text{II}}(\text{CN})_6]$ . By contrast, Glud-MFo revealed higher oxidation with the peaks moved to higher values. Interestingly, Glud-MFo exhibited similar peaks as Glup-MFi after GSH treatment, suggesting the central  $\text{Fe}^{\text{III}}$  had been reduced to  $\text{Fe}^{\text{II}}$  through GSH depletion. Moreover, the color of the powder changed from brown to grey-white further indicated the depletion ability of Glud-MFo (inset of Figure 2h). Furthermore, hydrogen-nuclear magnetic resonance ( $^1\text{H}$  NMR) spectra indicated a gradual generation of glutathione disulfide (GSSG) from GSH with the addition of Glud-MFo (Figure 2i). Total conversion to GSSG after 24 h was witnessed from  $^1\text{H}$  NMR spectra, fitting well with commercially available GSSG (Figure S4).<sup>19</sup> It is notable that under

acidic and high GSH conditions, the supernatant showed no further assemblies, suggesting the complete disassembly of two MOFs in response to these stimuli. As low pH value and high GSH concentration are typical characters of solid tumor, the ultrasensitive responsiveness of two MOFs to these stimuli endows their promise as smart nanocarriers for cancer treatment.<sup>43,44</sup>

**Synthesis of Glup-MFi-c and Glud-MFo-c.** Based on the robust coordination self-assembly of Glup-MFi and Glud-MFo, we further studied the feasibility of two MOFs for constructing photodynamic nanoagents. Chlorin e6 (Ce6), a photosensitizer with three carboxyl groups and one metal-binding chlorin ring was selected as a drug model, which can be encapsulated within two MOFs during the multicomponent self-assembly process. The addition of Ce6 during the synthesis process of two MOFs generated Glup-MFi-Ce6 (Glup-MFi-c) and Glud-MFo-Ce6 (Glud-MFo-c) nanoagents. During the one-step self-assembly strategy, multicomponent driven forces contributed to the successful formation of desired products, which involve collective coordination, hydrophobic, and electrostatic interactions between bridging linkers, coordination polymer, photosensitizers, and metal ions. Both SEM and TEM images indicated that the Glup-MFi-c and Glud-MFo-c nanoagents consist of isolated crack-free particles of diameter 100 nm (Figures 3a,b and S5). As revealed by high-angle annular dark-field scanning transmission electron microscopy (HAADF-STEM) and energy-dispersive X-ray spectroscopy (EDS) analyses, Mn, Fe, O, N, and C elements are homogeneously distributed within the Glud-MFo-c nanoagent (Figure 3c). The average hydrophilic diameter of the Glud-MFo-c is  $124 \pm 6.2$  nm by dynamic light scattering (DLS) analysis (Figure 3d). The polydispersity index (PDI) value from DLS is  $0.36 \pm 0.04$ , further suggesting the homogeneous distribution of size. On account of the existence of outer biocompatible PVP polymer, both Glup-MFi-c and Glud-MFo-c nanoagents showed robust and long-term stability in PBS solution (Figures S6 and S7). DLS measurements indicated a negligible change in size for two nanoagents even for storing 12 days at 4 °C condition. In addition, both Glud-MFo and Glud-MFo-c nanoagents exhibited good stability without detectable degradation or aggregation when dispersed into Dulbecco's modified eagle medium, fetal bovine serum, and cell lysate buffer solution (Figure S8). Zeta potential tests showed that both Glud-MFo and Glud-MFo-c exhibited a negative surface potential of  $-14.9 \pm 0.8$  mV and  $-19.7 \pm 1.6$  mV, respectively (Figure 3e). This would permit high colloidal stability in dispersed solution and prolonged half-life time during the blood circulation.<sup>45</sup>

Benefiting from the one-pot *in situ* self-assembly of these MOFs at room temperature, Ce6 molecule can be internalized into the pores directly without complicated post-loading and purification procedures. Significantly, the Ce6 loading capacity was as high as  $32.8 \pm 1.3$  wt%

and the loading efficiency was calculated to be  $95.5 \pm 3.2\%$ . The value is higher than some of the current carrier-based delivery systems, typically less than 20 wt% (Table S1).<sup>46</sup> Such high Ce6 loading capacity should be assigned to the following aspects. During the self-assembly process, Ce6 molecule not only acts as the loading cargo, but also participates in the self-assembly process through multicomponent interactions. This is evident from the UV-vis-NIR spectra shown in Figure 3f. The main absorbance peak of Ce6 in Glud-MFo-c showed a red-shift as compared to pure Ce6, indicating the coordination interaction between Ce6 and Mn ion together with the  $\pi$ - $\pi$  stacking between chlorin ring and bridging linker. In addition, N<sub>2</sub> sorption measurements presented a decreased Brunauer-Emmett-Teller surface area of Glud-MFo-c ( $183.6 \text{ m}^2 \text{ g}^{-1}$ ) compared with that of Glud-MFo ( $756.4 \text{ m}^2 \text{ g}^{-1}$ ), suggesting the successful encapsulation of Ce6 (Figure 3g). The pore size distribution of Glud-MFo-c was much disordered than that of Glud-MFo (Figure S9). The seemingly contradictory phenomenon further suggested the incorporation of Ce6 molecule within the framework of MOFs. Next, we explored the pH-responsive drug release under mimic acidic tumor microenvironment. TEM images clearly showed that Glud-MFo-c remained the original morphology under neutral condition (pH = 7.4). In contrast, Glud-MFo-c degraded completely under an acidic condition (pH = 5.0) within 24 h incubation (Figure 3h). Additionally, the Ce6 release profiles were also studied. Compared with the low release profile under pH 7.4, Glud-MFo-c degraded at a higher rate under mildly acidic conditions of pH values of 6.5 and 5.0 (Figure 3i). The pH-responsive drug release is no doubt originated from the disassembly of the frameworks under acidic condition, thus leading to the release of loaded Ce6.

***In Vitro* Enhanced PDT through GSH Depletion.** Encouraged by the pH-responsive drug release property, *in vitro* PDT was performed. The intracellular uptake of Glud-MFo-c was studied by confocal laser scanning microscopy (CLSM) at pre-determined time points using Ce6 as a fluorescent agent (Figure S10). The Ce6 fluorescence gradually increased with the prolonged incubation time to 6 h, indicating the Glud-MFo-c could be efficiently internalized by 4T1 cells. To investigate the biocompatibilities of different formulations under dark conditions, standard MTT (3-(4,5-dimethylthiazol-2-yl)-2,5-diphenyltetrazolium bromide) assays were performed. Results showed that  $[\text{Fe}^{\text{III}}(\text{CN})_6]$ ,  $[\text{Fe}^{\text{II}}(\text{CN})_6]$ , Glup-MFi-c, and Glud-MFo-c did not cause obvious decrease in the cell viability to 4T1 cells after 24 h incubation (Figure S11). To evaluate the *in vitro* PDT efficiency, 4T1 and HeLa cells were treated with PBS, Ce6, Glup-MFi-c, and Glud-MFo-c and followed with 10 min exposure by 660-nm light-emitting diode (LED) light with a power density at  $10 \text{ mW cm}^{-2}$ . Both Glup-MFi-c and Glud-MFo-c showed enhanced killing ability compared to free Ce6 with limited PDT efficiency at

the tested concentrations (Figure 4a). The killing efficiency is 95% for Glud-MFo-c compared to 80% for Glup-MFi-c at a Ce6 incubation of 8 ppm. The same trend can be observed for HeLa cells. As uncovered by previous literature, the overproduced intracellular GSH in tumor cells acting as ROS scavengers would compromise the efficiency of PDT.<sup>47,48</sup> The enhanced PDT effect should be assigned to the GSH-depletion within the tumor cells. To verify this hypothesis, 4T1 cells were stained with Thiol-Tracker after receiving different treatments (control, Glup-MFi, Glud-MFo, and buthionine sulfoximine (BSO)). Herein, BSO is a commonly used inhibitor for intracellular GSH synthesis. The Glup-MFi group exhibited comparable fluorescence intensity to the control group, indicating the GSH-passivation ability of  $[\text{Fe}^{\text{II}}(\text{CN})_6]$  (Figure 4b). In contrast, cells treated with Glud-MFo MOFs exhibited significantly decreased fluorescence, showing comparable GSH-depletion ability to BSO (Figure 4c).

To quantitatively analyze the change of intracellular GSH after different treatments, GSH fluorescent assay kits were applied. The results in Figure S12 showed that the initial concentration of intracellular GSH in 4T1 cells was measured to be  $6.6 \pm 0.5$  mM. After treated with Glud-MFo, the value of intracellular GSH decreased to  $2.7 \pm 0.5$  mM. When treated with BSO at a concentration of 10 ppm (0.045 mM), the intracellular GSH was significantly reduced to a value of  $0.8 \pm 0.1$  mM. Moreover, after treated with Glud-MFo,  $8 \times 10^6$  4T1 cells were collected to study the number of nanoparticles internalized per cell. The results showed that about 1,036 Glud-MFo nanoparticles were internalized per cell (see Supporting Information for more details). Herein, it should be noted that merely consuming intracellular GSH would not affect or slightly affect the survival of cells. BSO showed no killing effect on 4T1 cells at tested concentrations for 24 h (Figure S13). This is consistent with previous reports that BSO had a low cytotoxicity within a wide range of concentrations (0.1, 0.2, 1.0, and even 5 mM).<sup>49,50</sup> Herein, GSH depletion acts as an amplifier and can only play its synergistic role when combined with generated ROS for enhanced oxidative toxicity.

We further studied the lethal mechanism after different treatments. 4T1 cells treated with different groups were further stained by propidium iodide (PI) and annexin V-FITC double-staining and followed by flow cytometry analysis. The percentage of late apoptosis cells that truly reflect the ultimate cell death is the largest (68.8%) in the Glud-MFo-c group (Figure 4d). This result unambiguously demonstrates the GSH-depletion enhanced PDT efficiency of Glud-MFo-c. The same tendency can be observed through dead/live staining, in which cells were stained with calcein-AM and PI to differentiate dead and viable cells (Figure 4e). To further demonstrate ROS generation efficiency, 2,7-dichlorofluorescein diacetate (DCFH-DA) was qualitatively used as an intracellular ROS indicator. Results showed cells treated with Glud-

MFo-c exhibited the highest ROS level compared with Glup-MFi-c under the same irradiation conditions (Figure S14). It should be noted that Glud-MFo-c nanoagent showed negligible cytotoxicity to human embryo kidney (HEK293) normal cells under dark conditions (Figure S15). Under the irradiation of 660 nm LED light, however, Glud-MFo-c also exhibited concentration-dependent killing efficiency toward HEK293, similar to that of 4T1 cancerous cells under light irradiation. This means that one can apply the light irradiation only to cancerous tissues, while avoiding potential damages to normal tissues. The above results demonstrated that the Glud-MFo-c nanoagent could act as a ROS amplifier through GSH-depletion for enhanced PDT performance.

***In Vivo* Fluorescence and MR Imaging.** Motivated by the satisfying *in vitro* therapeutic results, we further explored *in vivo* performance of Glud-MFo-c nanoagent. Firstly, the half-life times of both free Ce6 and Glud-MFo-c during the blood circulation were determined *via* measuring the Ce6 concentration in the blood of mice after intravenous injection. The results showed that the calculated half-life time for Glud-MFo-c nanoagent in mouse blood was  $4.9 \pm 0.5$  h, much higher than that ( $2.9 \pm 0.3$  h) of free Ce6 (Figure S16), suggesting the good stability and long-term blood circulation of Glud-MFo-c nanoagent *in vivo*. Thereafter, *in vivo* fluorescence imaging was performed on 4T1 tumor cell-bearing mice through intravenous injection of free Ce6 or Glud-MFo-c (dose based on Ce6 is  $4 \text{ mg kg}^{-1}$ ) to study their tumor accumulation ability. The fluorescence within the tumor site of Glud-MFo-c group increased greater than that of the free Ce6 group, suggesting the enhanced tumor accumulation through the EPR effect (Figure 5a).<sup>8</sup> At 24 h post-injection, mice were sacrificed for *ex vivo* fluorescence imaging. As shown in Figure 5b, the tumor from Glud-MFo-c group was found to exhibit the strongest fluorescence, much higher than the fluorescence from main organs such as kidney, lung, spleen, liver, and heart, owing to the highest tumor accumulation of Glud-MFo-c nanoagent. Tumors from free Ce6 group showed much weaker fluorescence since free Ce6 is a small molecule with light molecular weight and it could be cleaned quickly from the body through metabolism.<sup>51,52</sup> Additionally, semi-quantitative fluorescence analysis of the main organs and tumor also indicated the enhanced tumor accumulation of Glud-MFo-c (Figure 5c). Notably, the liver and kidney of Glud-MFo-c group showed higher fluorescence compared to the free Ce6 group, indicating the liver decomposition of Glud-MFo-c and then clearance through the kidney system. As one  $[\text{Fe}^{\text{III}}(\text{CN})_6]$  linker is coordinated with six Mn ions to form octahedral  $\text{Mn}_6\text{-}[\text{Fe}(\text{CN})_6]$  ( $S = 5/2$ ) with high-spin state, thus Glud-MFo-c should be a suitable candidate for  $T_1$ -weighted MR imaging. MR imaging ability of Glud-MFo-c was performed on a clinical magnetic resonance scanner, showing a concentration-dependent effect in signal

intensity (Figure 5d). As shown in Figure 5e, the longitudinal relaxivity ( $r_1$ ) value was measured to be  $6.02 \pm 0.18 \text{ mM}^{-1} \text{ s}^{-1}$ , even better than clinically used Magnevist ( $r_1 = 4.56 \pm 0.23 \text{ mM}^{-1} \text{ s}^{-1}$ ).<sup>53</sup> *In vivo* MR imaging results exhibited time-dependent tumor accumulation behavior of Glud-MFo-c with brighter signals within 24 h post-injection (Figure 5f). Quantitative analysis further confirmed that the average MR imaging signal intensity within the tumor site increased over time (Figure 5g).

***In Vivo* Safety Assessment.** Before performing *in vivo* therapy, the biocompatibility of Glud-MFo-c was explored. The hemolysis test was performed, showing no visible hemolytic effects (<2%) within the tested ranges (Figure S17). It is notable that  $[\text{Fe}^{\text{III}}(\text{CN})_6]$  bridging linker is one of the building blocks of U.S. FDA approved drug Prussian blue, which is constructed by ferrous ion and  $[\text{Fe}^{\text{III}}(\text{CN})_6]$  bridging linker.<sup>35,54</sup> Furthermore, the main organs from mice injected with PBS (as control) and Glud-MFo-c were collected for hematoxylin and eosin (H&E) staining to study possible systemic toxicity (Figure 5h). Both control and Glud-MFo-c groups showed negligible pathological abnormalities or inflammations in main organs (heart, liver, spleen, lung, kidney, and intestine), favoring its biological safety as a theranostic agent. These results further demonstrate the feasibility and biosafety of Glud-MFo-c nanoagent, promising its future clinical translation.

***In Vivo* Antitumor Efficacy.** Motivated by the perfect *in vitro* photodynamic performance, *in vivo* therapy was also studied. 4T1 tumors bearing Balb/c mice were divided into four groups randomly ( $n = 5$ ): control group, free Ce6 group, Glup-MFi-c group, and Glud-MFo-c group. Compared with control and free Ce6 groups, the Glup-MFi-c group showed only partial tumor growth inhibition (Figure 6a). The group treated with Glud-MFo-c presented enhanced tumor suppression (Figures 6b and S18). All tumors were harvested after the treatment. The average weight of tumors from the Glud-MFo-c group was only 0.18 g, much lower than other groups (Figure 6c). No distinct variation of body weights was found for all mice (Figure S19). As compared to the Glup-MFi-c group, the enhanced therapeutic efficacy achieved by Glud-MFo-c should be assigned to a synergistic effect of GSH-depletion. Terminal deoxynucleotidyl transferase dUTP nick end label (TUNEL) staining demonstrated the highest apoptosis level for the Glud-MFo-c group with the brightest green fluorescence (Figure 6d). The quantitative intensity of green fluorescence for the Glud-MFo-c group was measured to be 72.3%, which was much higher than the Glup-MFi-c group (33.8%) and free Ce6 group (11.7%), suggesting its enhanced antitumor activity through GSH depletion (Figure 6e). Moreover, hematoxylin and eosin staining revealed a markedly higher apoptotic rate in the tumor tissue upon Glud-MFo-c treatment (Figure S20). To further evaluate the systematic safety, blood biochemical and

hematological indexes were analyzed. Results showed that the tested indexes of mice treated with Glud-MFo-c showed a little fluctuation on day 2, especially for ALP and ALT levels, which were ~2.37 and 2.92 times higher than those of the control group. However, no long-term side effects of Glud-MFo-c were observed over 16 days post-injection (Figure 6f). It should be noted that all the tested values were followed within the normal ranges.<sup>55</sup> The above results further demonstrated the feasibility and safety of Glud-MFo-c to mice using intravenous injection.

## CONCLUSIONS

Self-assembly is a promising strategy for constructing therapeutic nanoagents for personalized, effective, and noninvasive cancer treatment, as it integrates the adaptability of self-assembly and the simplicity of spatiotemporal control over cargo delivery. In this work, we have rationally developed two self-assembled nanoagents (Glup-MFi-c and Glud-MFo-c) for a comprehensive understanding of the GSH-depletion enhanced PDT. The self-assembled nanoagents can be readily constructed through cooperative coordination of short organic linkers and photosensitizers in the presence of metal ions, with uniform size and impressive *in situ* Ce6 encapsulation capacity. Glud-MFo-c presents robust stability under physiological conditions as well as rapid pH-responsive degradation and GSH-depletion capacity. The intrinsic microstructure of Mn-N<sub>6</sub> endows the self-assembled system with an excellent MR imaging property, which can be used for *in vivo* tracking. Due to the prolonged blood circulation time, more nanoparticles can be accumulated within the tumor site, ensuring enhanced antitumor efficiency as compared to free photosensitizers. These features promise the self-assembled nanoagents with efficient tumor ablation ability and negligible side-effects.

Compared with the existing GSH-depletion based therapeutic strategies, in this study, we have provided solid evidence for the GSH-depletion enhanced tumor therapy by designing a GSH-passivated system (Glup-MFi-c). Our results show that Glud-MFo-c can significantly inhibit tumor growth *in vivo* with negligible side-effect or toxicity. Because many anticancer drugs contain metal ion binding motifs, the present one-pot self-assembly strategy can be applied for other metal ions, photosensitizers, and also chemotherapy drugs. Importantly, due to the full utilization of all attended building blocks, systematic side-effects can be minimized. This study not only offers a strategy for the design of intracellular ROS-amplified tumor therapy but also offers a general guideline for constructing anticancer agents through targeting intracellular GSH.

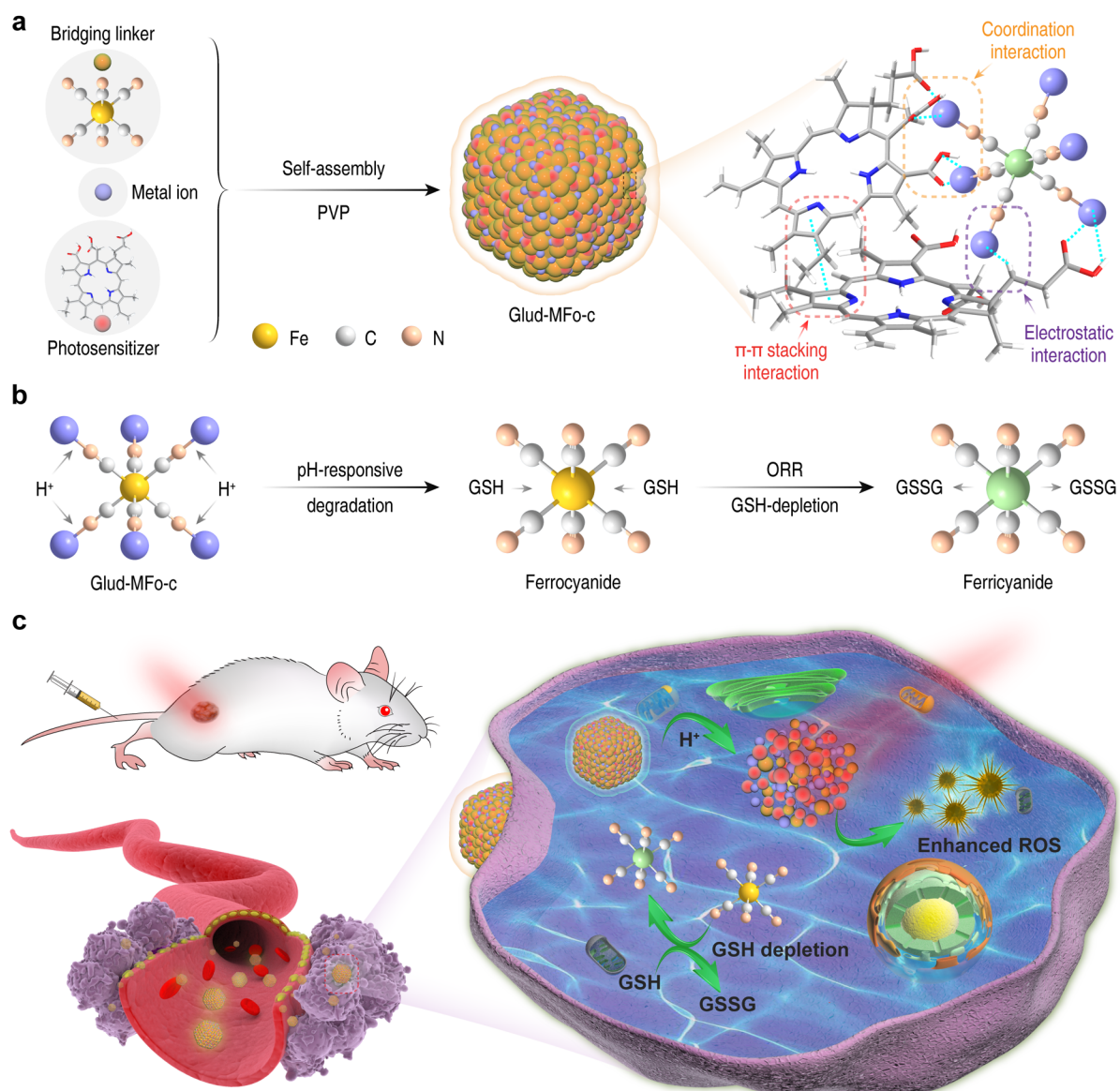


**Figure 1.** Schematic diagram of self-assembly Glud-MFo-c nanoagent for enhanced antitumor of PDT by Ce6 *via* GSH depletion. (a) Synthesis of Glud-MFo-c nanoagent. The formation is driven through cooperative coordination of bridging linkers, photosensitizers, and metal ions with the protection of outer PVP polymer. (b) The pH-responsive degradation mechanism and GSH-depletion through the oxidation-reduction reaction (ORR) between bridging linkers and intracellular over-expressed GSH. (c) Accumulation of Glud-MFo-c nanoagent in tumor site and the following cellular internalization, burst release of building blocks under acidic tumor microenvironments, and subsequent GSH-depletion for enhanced PDT efficiency.



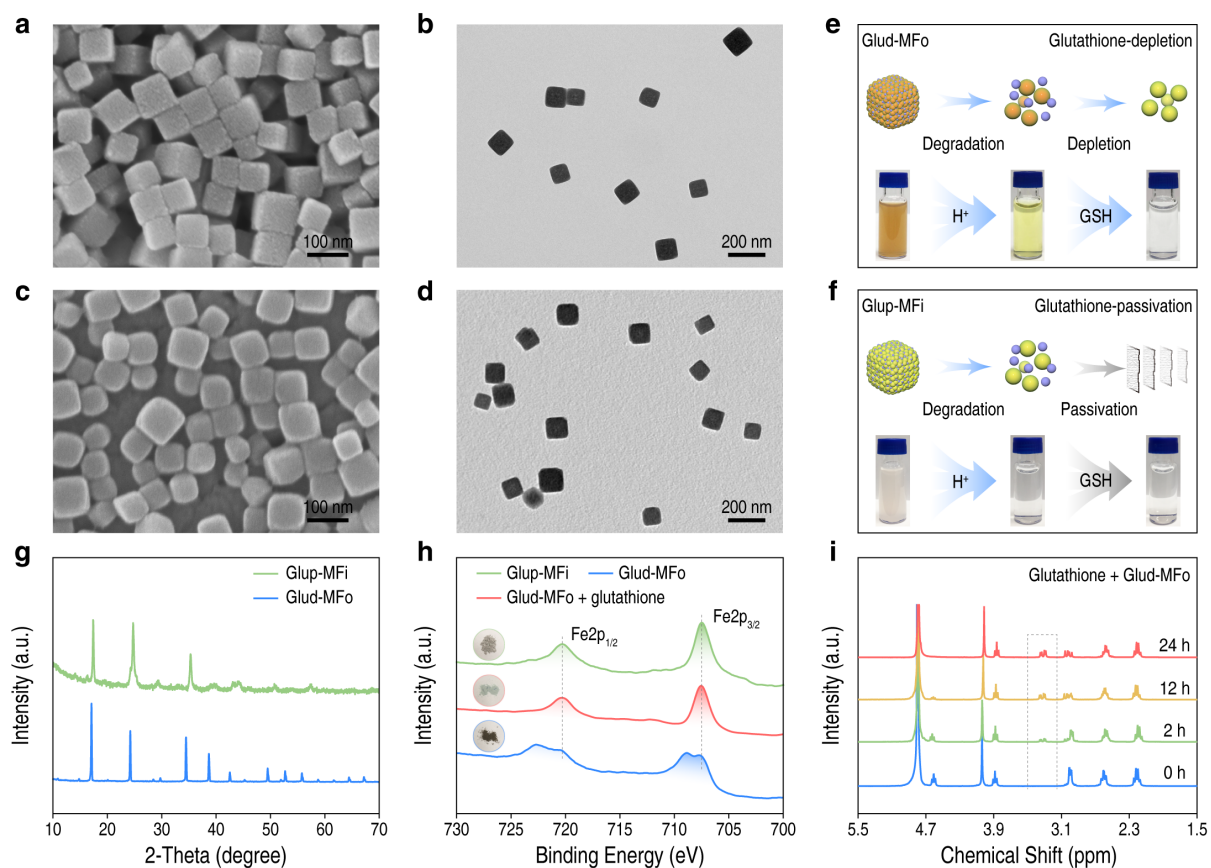


**Figure 2.** Characterizations of Glup-MFi and Glud-MFo nanoparticles. (a,b) SEM and TEM images of Glud-MFo. (c,d) SEM and TEM images of Glup-MFi. (e,f) Schematic illustration and photos showing the pH-response degradation of Glud-MFo and Glup-MFi, GSH-depletion of Glud-MFo, and GSH-passivation of Glup-MFi. (g) Powder XRD diffraction patterns of as-prepared Glup-MFi and Glud-MFo. (h) XPS Fe 2p spectra of Glup-MFi, Glud-MFo, and Glud-MFo after GSH treatment. (i)  $^1\text{H}$  NMR spectra of GSH after Glud-MFo treatment for different times.

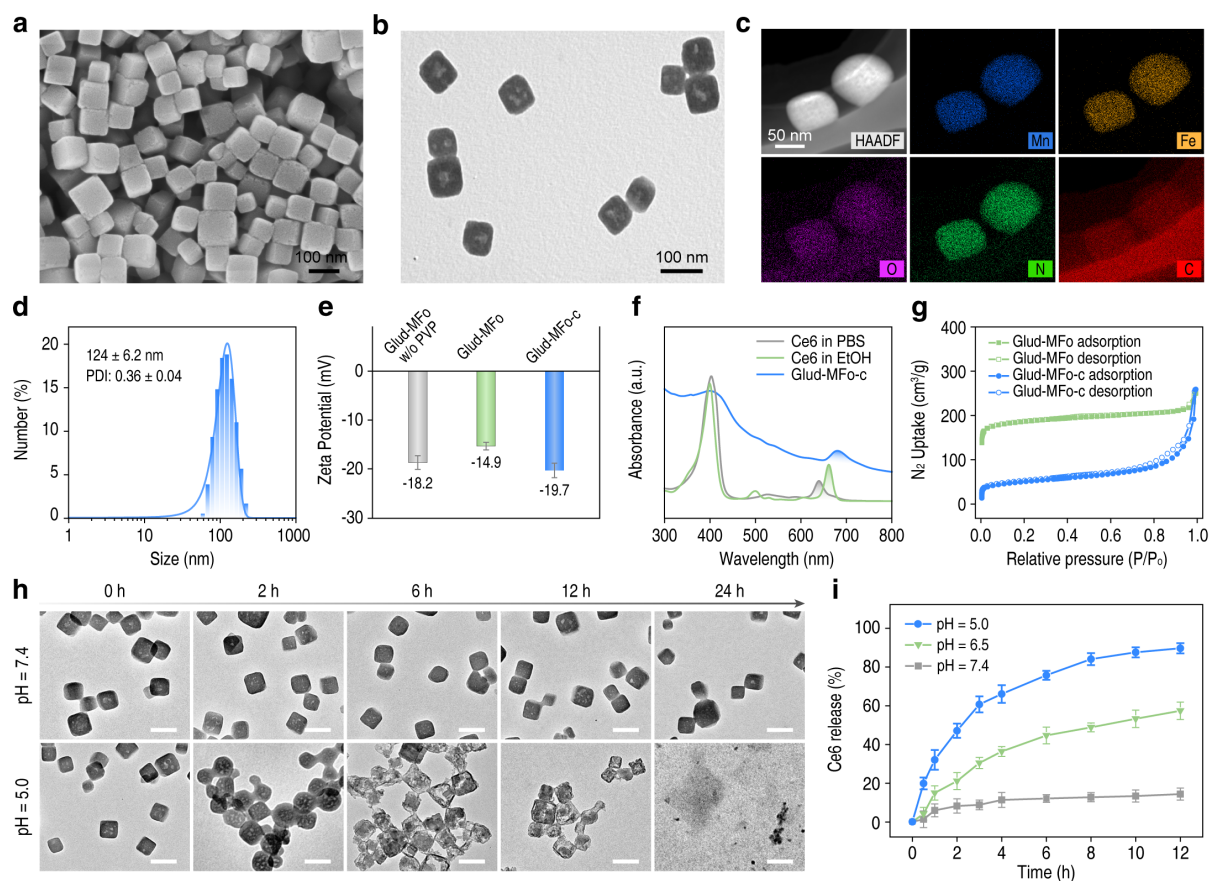


**Figure 3.** Characterizations of self-assembled Glud-MFo-c nanoagent. (a,b) SEM and TEM images of Glud-MFo-c nanoagent. (c) High-angle annular dark-field scanning transmission electron microscopy (HAADF-STEM) and energy-dispersive X-ray spectroscopy (EDS) elemental mapping of Glud-MFo-c nanoagent. (d) DLS profile of Glud-MFo-c nanoagent dispersed into PBS solution. (e) Zeta potential of Glud-MFo without PVP polymer, Glud-MFo, and Glud-MFo-c nanoagent. (f) UV-vis-NIR absorption spectra of free Ce6 and Glud-MFo-c nanoagent dispersed in PBS and ethanol. (g) Nitrogen sorption isotherms of Glud-MFo and Glud-MFo-c. (h) TEM images of Glud-MFo-c after incubation in PBS solutions with different pH values (7.4 and 5.0) for different times. The scale bar is 100 nm. (i) pH-Responsive Ce6 release profiles of Glud-MFo-c under different pH values.

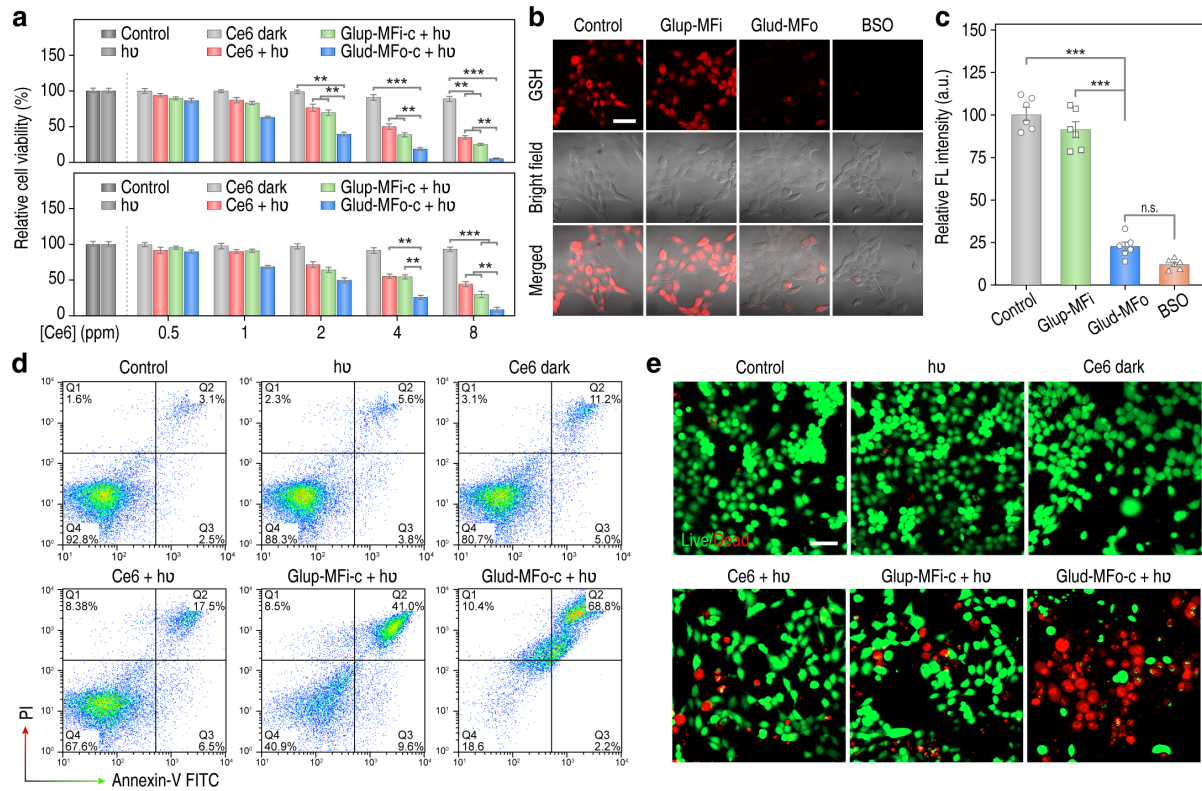


**Figure 4.** *In vitro* PDT assessments. (a) Relative cell viabilities of 4T1 (upper) and HeLa (down) cells after incubation with PBS, Ce6, Glup-MFi-c, and Glud-MFo-c for 4 h and then irradiated by 660 nm LED light ( $10 \text{ mW cm}^{-2}$ , 10 min). (b) Confocal images of 4T1 cells after different treatments and then stained with intracellular GSH assay. The scale bar is 50  $\mu\text{m}$ . (c) Relative fluorescence intensity of different groups after GSH assay. (d) Flow cytometry analysis of 4T1 cells after different treatments stained with annexin V-FITC/PI. (e) Live/dead double-staining of 4T1 cells after different treatments indicated by calcein-AM (green, live cells) and PI (red, dead cells). The scale bar is 50  $\mu\text{m}$ .

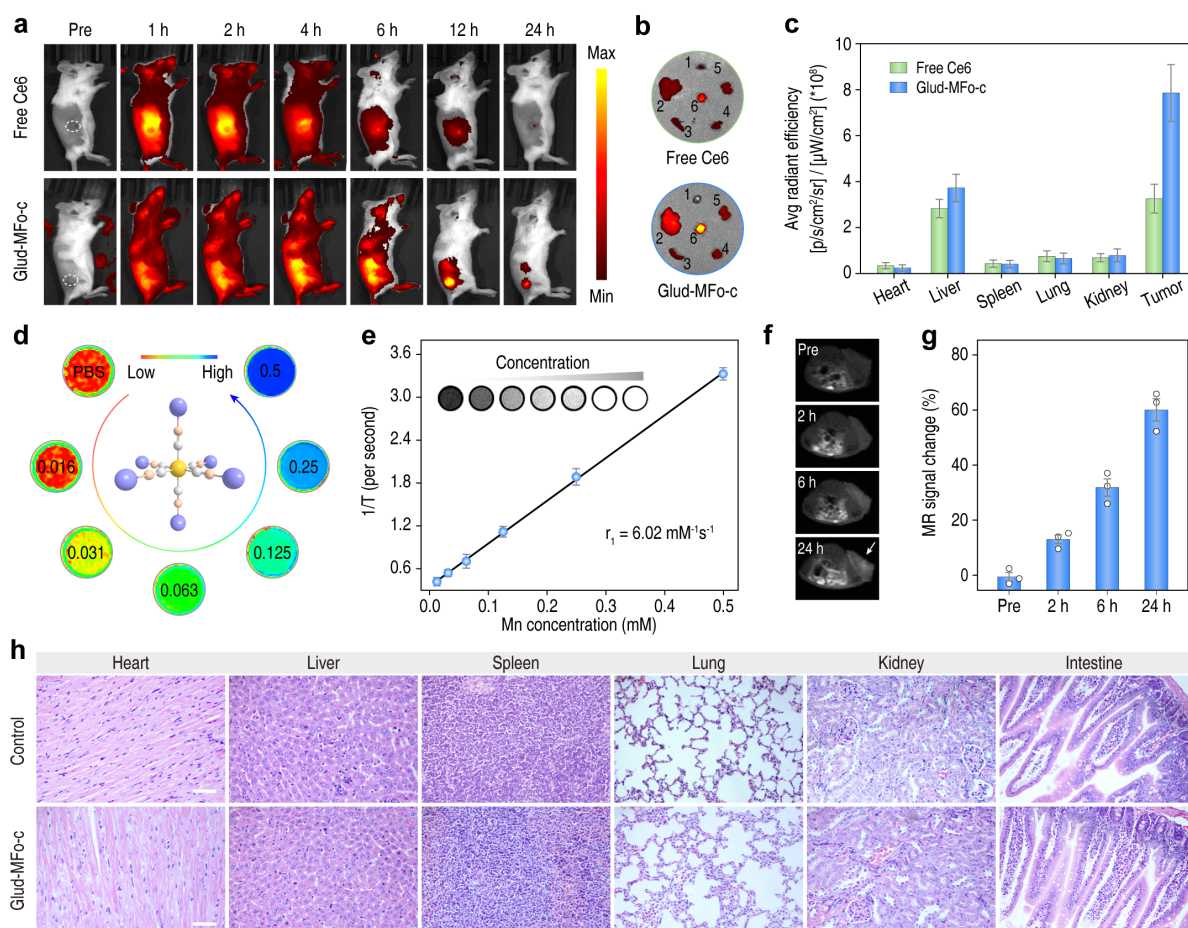


**Figure 5.** Fluorescence and MR imaging of Glud-MFo-c nanoagent. (a) *In vivo* fluorescence imaging of Glud-MFo-c nanoagent and free Ce6 at indicated time points after intravenous injection. (b) *Ex vivo* fluorescence image of main organs and tumor excised from mice at 24 h. 1, 2, 3, 4, 5, and 6 represent heart, liver, spleen, lung, kidney, and tumor, respectively. (c) Average radiant efficiency of the organs and tumors. (d) *In vitro*  $T_1$ -weighted MR images of Glud-MFo-c in aqueous solution of various Mn concentrations. (e) Linear plot of  $1/T_1$  as a function of Mn concentration. The inset is  $T_1$ -weighted MR phantom recorded using 3T MR scanner. (f) *In vivo* MR images of tumor-bearing mouse at 0 h, 2 h, 6 h, and 24 h post-injection. Tumor site is indicated by the arrow. (g) Quantitative analyses of  $T_1$ -weighted MR signals of the tumor. (h) Hematoxylin and eosin (H&E) staining of major organs after administrated with PBS and Glud-MFo-c nanoagent. The scale bar is 50  $\mu\text{m}$ .



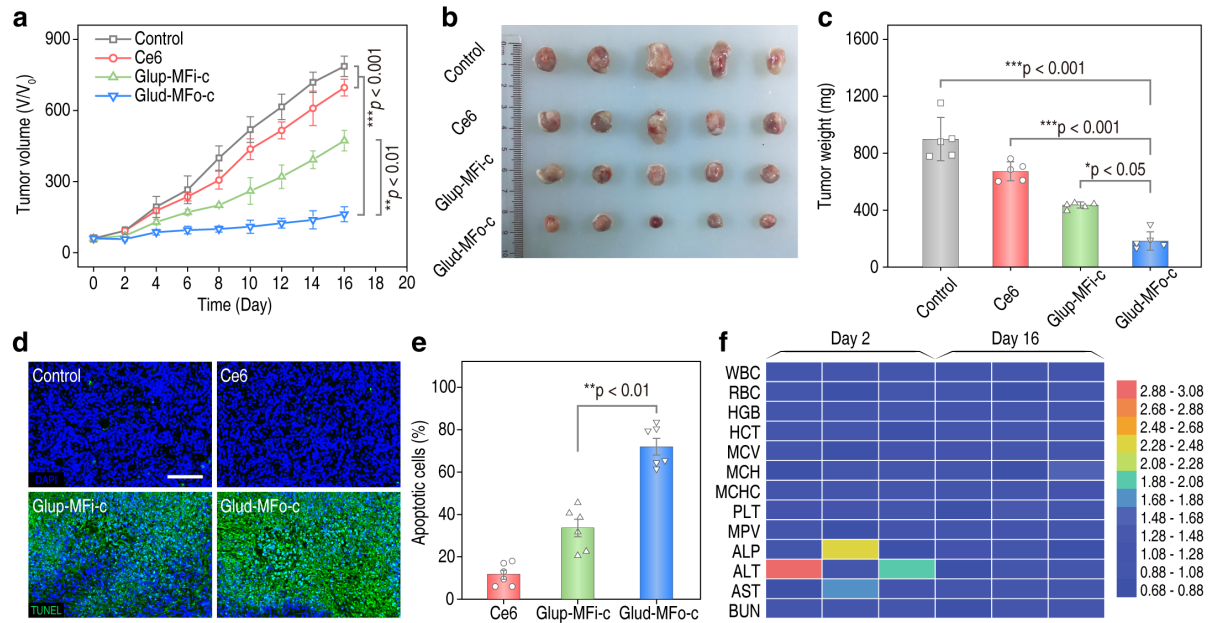


**Figure 6.** *In vivo* PDT assessments. (a) Tumor growth curves of different groups (Control, Ce6, Glup-MFi-c, and Glud-MFo-c) during the treatments. (b) Photograph of tumors excised from the mice at the end of the treatments. (c) Average weights of tumors harvested at the end of treatment (n = 5). (d) TdT-mediated dUTP nick-end labeling (TUNEL) staining of tumor sections at the end of treatment. Nuclei were stained with DAPI (blue) and TUNEL (green). The scale bar is 100 μm. (e) Relative apoptotic percentage of cells determined by fluorescent TUNEL staining. (f) Hematological indexes and biochemical analyses of mouse blood, where the mice were intravenously injected with PBS and Glud-MFo-c for 2 and 16 days.

## EXPERIMENTAL SECTION

**Synthesis of Glud-MFo-c and Glup-MFi-c.** For the synthesis of self-assembled Glud-MFo-c or Glup-MFi-c nanoagent,  $K_3[Fe^{III}(CN)_6]$  (0.1 mmol) or  $K_4[Fe^{II}(CN)_6]$  (0.1 mmol), PVP (0.3 g) and Ce6 (10 mg, pre-dissolved in 0.1 M NaOH solution to neutralize -COOH group) were dispersed in water/ethanol (15/5 mL) mixed solution. Subsequently,  $Mn(CH_3COO)_2 \cdot 4H_2O$  (0.2 mmol) or  $MnSO_4 \cdot H_2O$  (0.2 mmol) and dispersed in water (10 mL) were added dropwise with continuous stirring. Turbidity generated immediately upon the addition of metal ions. Thereafter, the reaction was maintained for 24 h under stirring. The fabrication of Glud-MFo and Glup-MFi follows the same procedure without Ce6. Final products were collected with centrifugation for characterizations.

**GSH-Depletion Assessment.** For GSH-depletion, Glup-MFi and Glud-MFo (10 mg) were added into GSH solution (10 mM) and maintained for 24 h. The precipitates were centrifuged and collected for XPS characterization. Time-dependent GSH-depletion was performed by mixing Glud-MFo MOFs with pure GSH in  $D_2O$  solution. At different time points, supernatants were collected for  $^1H$  NMR (300 MHz) characterization.

**pH-Responsive Release of Ce6.** A typical release system was prepared by suspending Glud-MFo-c (10 mg) in PBS solutions with different pH values (20.0 mL, pH = 7.4, 6.5, and 5.0, respectively). The release system was then maintained at 37 °C under shaking. 1 mL of release medium was sampled at each time point, and UV-vis-NIR spectrophotometry was used to determine the percentage of the released Ce6, after which the sample was returned to the original release system. The release percentages of Ce6 were calculated according to the formula, release percentage (%) =  $m_s/m_t$ , where  $m_s$  is the amount of free Ce6 in the supernatant, and  $m_t$  is the total amount of loaded Ce6.

**Cellular Uptake and *In Vitro* Therapy.** Murine breast (4T1) cancer cells, human cervical (HeLa) cancer cells, and human embryo kidney (HEK293) normal cells were originally obtained from the American Type Culture Collection (ATCC). For cellular uptake, 4T1 cells were seeded on chambered coverglass (Lab-Tek Chambered Coverglass, Nunc) and incubated with Glud-MFo-c. After co-incubation for 1 h, 2 h, and 6 h, the cells were further stained with 4,6-diamidino-2-phenylindole (DAPI) and Lyso-Tracker before performing confocal laser scanning microscopy (ZEISS LSM 800) to study the time-dependent internalization. For *in vitro* therapy, different cells were cultured in 96-well plates at  $1 \times 10^4$  cells/well and incubated in 5%  $CO_2$  at 37 °C for 24 h. For biocompatibility assessments, different concentrations of BSO, Glup-MFi MOF, Glud-MFo MOF, and Glud-MFo-c nanoagent were incubated with cells. The biocompatibility of two bridging linkers were tested with the same procedure at different

incubation concentrations (0 to 200 ppm). For enhanced PDT, 4T1 and HeLa cancer cells were seeded into 96-well plates and then incubated with a range of concentrations of free Ce6, Glup-MFi-c, and Glud-MFo-c nanoagent (with equivalent Ce6 concentration from 0 to 8 ppm) at 37 °C. After incubation for 4 h, 4T1 and HeLa cells were exposed to 660-nm LED light irradiation (10 mW cm<sup>-2</sup>, 10 min). Cell viabilities were determined by the standard MTT method.

**Intracellular GSH-Depletion.** 4T1 cells were seeded on chambered coverglass (Lab-Tek Chambered Coverglass, Nunc). After treating with PBS, Glup-MFi, Glud-MFo, and BSO for 12 h. Thereafter, 4T1 cells were washed with PBS before staining with intracellular Thiol-Tracker agent. After washing with PBS for three times, the cells were imaged under confocal microscopy for observing the GSH level. To quantitatively study the intracellular GSH concentrations of 4T1 cells after different treatments, 2×10<sup>6</sup> cells from each group were collected for intracellular GSH fluorescent assay (see Supporting Information for details). To estimate the number of Glud-MFo-c nanoparticles in each 4T1 cell, inductively coupled plasma mass spectrometry measurement was performed to test Fe species in 8×10<sup>6</sup> cells (see Supporting Information for details).

**Intracellular ROS Detection.** 4T1 cells were seeded on chambered coverglass (Lab-Tek Chambered Coverglass, Nunc). After treating with free Ce6, Glup-MFi-c, and Glud-MFo-c followed by light irradiation (10 mW cm<sup>-2</sup>, 10 min), the cellular ROS levels were measured by ROS assay kit (DCFH-DA, Invitrogen™) using confocal microscopy.

**In Vivo Fluorescence Imaging.** For *in vivo* fluorescence imaging, the mice were first administrated with free Ce6 and Glud-MFo-c nanoagent through intravenous injection (equivalent concentration of Ce6 is 4 mg kg<sup>-1</sup>). Imaging was performed at different time points upon injection with a 676 nm excitation wavelength on *in vivo* optical imaging system (IVIS spectrum-CT *In Vivo* Imaging System). After imaging, mice were sacrificed for the harvest of main organs such as heart, liver, spleen, lung, kidney, and tumor for studying the biodistribution of Ce6. Furthermore, the half-life times of both free Ce6 and Glud-MFo-c nanoagent in blood circulation were studied. Free Ce6 and Glud-MFo-c (equivalent Ce6 dose, 4 mg/kg) were injected into mice through tail vein. At pre-determined time points, 20 µL blood sample was extracted to study the fluorescence of Ce6.

**Magnetic Resonance Imaging.** Glud-MFo-c at different Mn concentrations (0 to 0.5 mM) was measured at 25 °C with a clinical MR scanner (GE HDxt, 3.0 T). For *in vivo* MR imaging, 4T1 tumor-bearing mice (n = 3) with an average body weight of 20 g (Shanghai SLAC Laboratory Animal Co., Ltd.) were conducted. T<sub>1</sub>-weighted MR images were acquired under pre-injection, 2 h, 6 h, and 24 h post-injection of Glud-MFo-c saline solution (12.2 mg kg<sup>-1</sup>).

T<sub>1</sub>-weighted MR images were acquired using a fast spin-echo multi-slice (f-SEMS) sequence with parameters: TR/TE = 780/19.6 ms, number of excitations = 2, an echo train length = 2, 0.188 × 0.188 mm in-plane resolution with a slice thickness of 2 mm.

***In Vivo* Biocompatibility Analysis.** After *in vivo* imaging, the mice were used to analyze the long-term biocompatibility. The mice were euthanized and the main organs of the mice (heart, kidney, liver, lung, spleen, and intestine) were harvested and fixed using 4% paraformaldehyde. Tissue samples were then embedded in paraffin, sliced (4 μm), and stained for further histological analysis by standard hematoxylin and eosin (H&E) staining procedure.

***In Vivo* Antitumor Study.** 4T1 tumor mice were established for xenograft experiments, and they were randomly allocated into four groups (n = 5): Control, free Ce6, Glup-MFi-c, Glud-MFo-c. When the tumor volume reached 50 ~ 60 mm<sup>3</sup>, Ce6, Glup-MFi-c and Glud-MFo-c in saline solution (injection dose = 100 μL, the equivalent concentration of Ce6 is 4 mg kg<sup>-1</sup>) were injected *via* the tail vein. At 6 h post intravenous injection, groups of free Ce6, Glup-MFi-c, and Glud-MFo-c were subjected to light irradiation (660-nm LED light, 10 mW cm<sup>-2</sup>, 20 min). Mice in the control group were only injected with saline. Tumor dimensions were measured every two days with a caliper. The tumor volume was calculated according to the equation: Volume = (Tumor length) × (Tumor width)<sup>2</sup>/2 (mm<sup>3</sup>). At the end of the treatment, all mice were sacrificed and tumors were collected and weighted.

**Biochemical Analysis of Blood.** Mice without tumor (n = 3) were treated with PBS or Glud-MFo-c through intravenous injection. On day 2 and day 16 after injection, blood samples were collected. For blood routine analysis, parameters such as white blood cell, red blood cells, hemoglobin, hematocrit, mean corpuscular volume, mean corpuscular hemoglobin, mean corpuscular hemoglobin concentration, platelets, and mean platelet volume were measured. For the blood biochemistry test, alkaline phosphatase, alanine transaminase, aspartate aminotransferase, and blood urea nitrogen serving as hepatic and renal function markers were measured.

## ASSOCIATED CONTENT

### Supporting Information

The Supporting Information is available free of charge *via* the Internet at <http://pubs.acs.org>.

Synthesis and characterization details, *in vitro* and *in vivo* experiment procedures, statistical analysis, powder XRD patterns, NMR spectra, SEM and TEM images, long-term stability measurements, comparison of Ce6 loading with other nanocarriers, surface area measurements,



CLSM images, *in vitro* biocompatibility, quantitative determination of intracellular GSH, nanoparticles internalization, cell viability of BSO, ROS staining, biocompatibility and killing efficiency of Glud-MFo-c to HEK293 normal cells, half-life times of free Ce6 and Glud-MFo-c in blood circulation, hemolysis of red blood cells, photos of mice, body weight of mice, and histopathology images (PDF)

## **AUTHOR INFORMATION**

### **Corresponding Author:**

**Yanli Zhao** - Division of Chemistry and Biological Chemistry, School of Physical and Mathematical Sciences, Nanyang Technological University, 21 Nanyang Link, Singapore 637371, Singapore;

School of Materials Science and Engineering, Nanyang Technological University, 50 Nanyang Avenue, Singapore 639798, Singapore;

School of Chemical and Biomedical Engineering, Nanyang Technological University, 70 Nanyang Drive, Singapore 637457, Singapore;

orcid.org/0000-0002-9231-8360; Email: zhaoyanli@ntu.edu.sg

**Zhen Guo** - Anhui Key Laboratory for Cellular Dynamics and Chemical Biology, School of Life Sciences, University of Science and Technology of China, Hefei 230027, P. R. China; Email: zhenguo@ustc.edu.cn

### **Authors:**

**Dongdong Wang** - Division of Chemistry and Biological Chemistry, School of Physical and Mathematical Sciences, Nanyang Technological University, 21 Nanyang Link, Singapore 637371, Singapore; orcid.org/0000-0002-6278-0706

**Huihui Wu** - Anhui Key Laboratory for Cellular Dynamics and Chemical Biology, School of Life Sciences, University of Science and Technology of China, Hefei 230027, P. R. China

**Guangbao Yang** - Division of Chemistry and Biological Chemistry, School of Physical and Mathematical Sciences, Nanyang Technological University, 21 Nanyang Link, Singapore 637371, Singapore; orcid.org/0000-0001-6180-5310

**Cheng Qian** - Division of Chemistry and Biological Chemistry, School of Physical and Mathematical Sciences, Nanyang Technological University, 21 Nanyang Link, Singapore 637371, Singapore; orcid.org/0000-0002-1392-6975

**Long Gu** - Division of Chemistry and Biological Chemistry, School of Physical and Mathematical Sciences, Nanyang Technological University, 21 Nanyang Link, Singapore 637371, Singapore; orcid.org/0000-0002-5576-031X

**Hou Wang** - Division of Chemistry and Biological Chemistry, School of Physical and Mathematical Sciences, Nanyang Technological University, 21 Nanyang Link, Singapore 637371, Singapore; orcid.org/0000-0002-2066-1856

**Weiqiang Zhou** - Division of Chemistry and Biological Chemistry, School of Physical and Mathematical Sciences, Nanyang Technological University, 21 Nanyang Link, Singapore 637371, Singapore;

**Jiawei Liu** - Division of Chemistry and Biological Chemistry, School of Physical and Mathematical Sciences, Nanyang Technological University, 21 Nanyang Link, Singapore 637371, Singapore; orcid.org/0000-0003-4011-3950

**Yinglong Wu** - Division of Chemistry and Biological Chemistry, School of Physical and Mathematical Sciences, Nanyang Technological University, 21 Nanyang Link, Singapore 637371, Singapore; orcid.org/0000-0002-4453-4827

**Xiaodong Zhang** - Division of Chemistry and Biological Chemistry, School of Physical and Mathematical Sciences, Nanyang Technological University, 21 Nanyang Link, Singapore 637371, Singapore; orcid.org/0000-0003-4137-3535

**Hongzhong Chen** - Division of Chemistry and Biological Chemistry, School of Physical and Mathematical Sciences, Nanyang Technological University, 21 Nanyang Link, Singapore 637371, Singapore

**Deblin Jana** - Division of Chemistry and Biological Chemistry, School of Physical and Mathematical Sciences, Nanyang Technological University, 21 Nanyang Link, Singapore 637371, Singapore

## **ACKNOWLEDGMENT**

This research is supported by the Singapore National Research Foundation Investigatorship (NRF-NRFI2018-03), the Singapore Academic Research Fund (RT12/19), the National Natural Science Foundation of China (31471268), and the National Key Research and Development Program of China (Stem Cell and Translational Research, 2016YFA0101202).

## REFERENCES

- (1) Dolmans, D. E. J. G. J.; Fukumura, D.; Jain, R. K. Photodynamic Therapy for Cancer. *Nat. Rev. Cancer* **2003**, *3*, 380-387.
- (2) Lucky, S. S.; Soo, K. C.; Zhang, Y. Nanoparticles in Photodynamic Therapy. *Chem. Rev.* **2015**, *115*, 1990-2042.
- (3) Agostinis, P.; Berg, K.; Cengel, K. A.; Foster, T. H.; Girotti, A. W.; Gollnick, S. O.; Hahn, S. M.; Hamblin, M. R.; Juzeniene, A.; Kessel, D.; Korbelik, M.; Moan, J.; Mroz, P.; Nowis, D.; Piette, J.; Wilson, B. C.; Golab, J. Photodynamic Therapy of Cancer: An Update. *Ca-Cancer J. Clin.* **2011**, *61*, 250-281.
- (4) Hopper, C. Photodynamic Therapy: A Clinical Reality in the Treatment of Cancer. *Lancet Oncol.* **2000**, *1*, 212-219.
- (5) Zhao, L.; Li, J.; Su, Y.; Yang, L.; Chen, L.; Qiang, L.; Wang, Y.; Xiang, H.; Tham, H. P.; Peng, J.; Zhao, Y. MTH1 Inhibitor Amplifies the Lethality of Reactive Oxygen Species to Tumor in Photodynamic Therapy. *Sci. Adv.* **2020**, *6*, eaaz0575.
- (6) Xu, S.; Zhu, X.; Zhang, C.; Huang, W.; Zhou, Y.; Yan, D. Oxygen and Pt(II) Self-Generating Conjugate for Synergistic Photo-Chemo Therapy of Hypoxic Tumor. *Nat. Commun.* **2018**, *9*, 2053.
- (7) Bump, E. A.; Yu, N. Y.; Brown, J. M. Radiosensitization of Hypoxic Tumor Cells by Depletion of Intracellular Glutathione. *Science* **1982**, *217*, 544-545.
- (8) Fang, J.; Nakamura, H.; Maeda, H. The EPR Effect: Unique Features of Tumor Blood Vessels for Drug Delivery, Factors Involved, and Limitations and Augmentation of the Effect. *Adv. Drug Deliv. Rev.* **2011**, *63*, 136-151.
- (9) Hobbs, S. K.; Monsky, W. L.; Yuan, F.; Roberts, W. G.; Griffith, L.; Torchilin, V. P.; Jain, R. K. Regulation of Transport Pathways in Tumor Vessels: Role of Tumor Type and Microenvironment. *Proc. Natl. Acad. Sci. U. S. A.* **1998**, *95*, 4607-4612.
- (10) Wang, D.; Wu, H.; Lim, W. Q.; Phua, S. Z. F.; Xu, P.; Chen, Q.; Guo, Z.; Zhao, Y. A Mesoporous Nanoenzyme Derived from Metal-Organic Frameworks with Endogenous Oxygen Generation to Alleviate Tumor Hypoxia for Significantly Enhanced Photodynamic Therapy. *Adv. Mater.* **2019**, *31*, 1901893.
- (11) Kuppusamy, P.; Li, H.; Ilangoan, G.; Cardounel, A. J.; Zweier, J. L.; Yamada, K.; Krishna, M. C.; Mitchell, J. B. Noninvasive Imaging of Tumor Redox Status and Its Modification by Tissue Glutathione Levels. *Cancer Res.* **2002**, *62*, 307-312.
- (12) Schafer, F. Q.; Buettner, G. R. Redox Environment of the Cell as Viewed through the Redox State of the Glutathione Disulfide/Glutathione Couple. *Free Radical Biol. Med.* **2001**,

30, 1191-1212.

(13) Su, L.; Li, R.; Khan, S.; Clanton, R.; Zhang, F.; Lin, Y. N.; Song, Y.; Wang, H.; Fan, J.; Hernandez, S.; Butters, A. S.; Akabani, G.; MacLoughlin, R.; Smolen, J.; Wooley, K. L. Chemical Design of Both a Glutathione-Sensitive Dimeric Drug Guest and a Glucose-Derived Nanocarrier Host to Achieve Enhanced Osteosarcoma Lung Metastatic Anticancer Selectivity. *J. Am. Chem. Soc.* **2018**, *140*, 1438-1446.

(14) Tai, D. J.; Jin, W. S.; Wu, C. S.; Si, H. W.; Cao, X. D.; Guo, A. J.; Chang, J. C. Changes in Intracellular Redox Status Influence Multidrug Resistance in Gastric Adenocarcinoma Cells. *Exp. Ther. Med.* **2012**, *4*, 291-296.

(15) Diehn, M.; Cho, R. W.; Lobo, N. A.; Kalisky, T.; Dorie, M. J.; Kulp, A. N.; Qian, D.; Lam, J. S.; Ailles, L. E.; Wong, M.; Joshua, B.; Kaplan, M. J.; Wapnir, I.; Dirbas, F. M.; Somlo, G.; Garberoglio, C.; Paz, B.; Shen, J.; Lau, S. K.; Quake, S. R. *et al.* Association of Reactive Oxygen Species Levels and Radioresistance in Cancer Stem Cells. *Nature* **2009**, *458*, 780-783.

(16) Gorrini, C.; Harris, I. S.; Mak, T. W. Modulation of Oxidative Stress as an Anticancer Strategy. *Nat. Rev. Drug Discovery* **2013**, *12*, 931-947.

(17) Chang, M.; Wang, M.; Wang, M.; Shu, M.; Ding, B.; Li, C.; Pang, M.; Cui, S.; Hou, Z.; Lin, J. A Multifunctional Cascade Bioreactor Based on Hollow-Structured Cu<sub>2</sub>MoS<sub>4</sub> for Synergetic Cancer Chemodynamic Therapy/Starvation Therapy/Phototherapy/Immunotherapy with Remarkably Enhanced Efficacy. *Adv. Mater.* **2019**, *31*, 1905271.

(18) Liu, C.; Cao, Y.; Cheng, Y.; Wang, D.; Xu, T.; Su, L.; Zhang, X.; Dong, H. An Open Source and Reduce Expenditure ROS Generation Strategy for Chemodynamic/Photodynamic Synergistic Therapy. *Nat. Commun.* **2020**, *11*, 1735.

(19) Ma, B.; Wang, S.; Liu, F.; Zhang, S.; Duan, J.; Li, Z.; Kong, Y.; Sang, Y.; Liu, H.; Bu, W.; Li, L. Self-Assembled Copper-Amino Acid Nanoparticles for *in Situ* Glutathione "AND" H<sub>2</sub>O<sub>2</sub> Sequentially Triggered Chemodynamic Therapy. *J. Am. Chem. Soc.* **2019**, *141*, 849-857.

(20) Gong, F.; Cheng, L.; Yang, N.; Betzer, O.; Feng, L.; Zhou, Q.; Li, Y.; Chen, R.; Popovtzer, R.; Liu, Z. Ultrasmall Oxygen-Deficient Bimetallic Oxide MnWO<sub>x</sub> Nanoparticles for Depletion of Endogenous GSH and Enhanced Sonodynamic Cancer Therapy. *Adv. Mater.* **2019**, *31*, 1900730.

(21) Zhang, H.; Liu, K.; Li, S.; Xin, X.; Yuan, S.; Ma, G.; Yan, X. Self-Assembled Minimalist Multifunctional Theranostic Nanoplatform for Magnetic Resonance Imaging-Guided Tumor Photodynamic Therapy. *ACS Nano* **2018**, *12*, 8266-8276.

(22) Gong, N.; Ma, X.; Ye, X.; Zhou, Q.; Chen, X.; Tan, X.; Yao, S.; Huo, S.; Zhang, T.; Chen, S.; Teng, X.; Hu, X.; Yu, J.; Gan, Y.; Jiang, H.; Li, J.; Liang, X. J. Carbon-Dot-Supported

Atomically Dispersed Gold as a Mitochondrial Oxidative Stress Amplifier for Cancer Treatment. *Nat. Nanotechnol.* **2019**, *14*, 379-387.

(23) Lu, Y.; Yang, Y.; Gu, Z.; Zhang, J.; Song, H.; Xiang, G.; Yu, C. Glutathione-Depletion Mesoporous Organosilica Nanoparticles as a Self-Adjuvant and Co-Delivery Platform for Enhanced Cancer Immunotherapy. *Biomaterials* **2018**, *175*, 82-92.

(24) Yu, Q.; Zhang, Y. M.; Liu, Y. H.; Xu, X.; Liu, Y. Magnetism and Photo Dual-Controlled Supramolecular Assembly for Suppression of Tumor Invasion and Metastasis. *Sci. Adv.* **2018**, *4*, eaat2297.

(25) Chen, H.; Zeng, X.; Tham, H. P.; Phua, S. Z. F.; Cheng, W.; Zeng, W.; Shi, H.; Mei, L.; Zhao, Y. NIR-Light-Activated Combination Therapy with a Precise Ratio of Photosensitizer and Prodrug Using a Host-Guest Strategy. *Angew. Chem., Int. Ed.* **2019**, *58*, 7641-7646.

(26) Wang, D.; Jana, D.; Zhao, Y. Metal-Organic Framework Derived Nanozymes in Biomedicine. *Acc. Chem. Res.* **2020**, *53*, 1389-1400.

(27) Cheng, G.; Li, W.; Ha, L.; Han, X.; Hao, S.; Wan, Y.; Wang, Z.; Dong, F.; Zou, X.; Mao, Y.; Zheng, S. Y. Self-Assembly of Extracellular Vesicle-Like Metal-Organic Framework Nanoparticles for Protection and Intracellular Delivery of Biofunctional Proteins. *J. Am. Chem. Soc.* **2018**, *140*, 7282-7291.

(28) Wu, M. X.; Yang, Y. W. Metal-Organic Framework (MOF)-Based Drug/Cargo Delivery and Cancer Therapy. *Adv. Mater.* **2017**, *29*, 1606134.

(29) Kitao, T.; Zhang, Y.; Kitagawa, S.; Wang, B.; Uemura, T. Hybridization of MOFs and Polymers. *Chem. Soc. Rev.* **2017**, *46*, 3108-3133.

(30) Wang, D.; Wu, H.; Zhou, J.; Xu, P.; Wang, C.; Shi, R.; Wang, H.; Wang, H.; Guo, Z.; Chen, Q. *In Situ* One-Pot Synthesis of MOF-Polydopamine Hybrid Nanogels with Enhanced Photothermal Effect for Targeted Cancer Therapy. *Adv. Sci.* **2018**, *5*, 1800287.

(31) Chen, G.; Huang, S.; Kou, X.; Wei, S.; Huang, S.; Jiang, S.; Shen, J.; Zhu, F.; Ouyang, G. A Convenient and Versatile Amino-Acid-Boosted Biomimetic Strategy for the Nondestructive Encapsulation of Biomacromolecules within Metal-Organic Frameworks. *Angew. Chem. Int. Ed.* **2019**, *58*, 1463-1467.

(32) Kaye, S. S.; Long, J. R. Hydrogen Storage in the Dehydrated Prussian Blue Analogues  $M_3[Co(CN)_6]_2$  ( $M = Mn, Fe, Co, Ni, Cu, Zn$ ). *J. Am. Chem. Soc.* **2005**, *127*, 6506-6507.

(33) Simonov, A.; De Baerdemaeker, T.; Bostrom, H. L. B.; Rios Gomez, M. L.; Gray, H. J.; Chernyshov, D.; Bosak, A.; Burgi, H. B.; Goodwin, A. L. Hidden Diversity of Vacancy Networks in Prussian Blue Analogues. *Nature* **2020**, *578*, 256-260.

(34) Wang, D.; Wu, H.; Phua, S. Z. F.; Yang, G.; Lim, W. Q.; Gu, L.; Qian, C.; Wang, H.;

Guo, Z.; Chen, H.; Zhao, Y. Self-Assembled Single-Atom Nanozyme for Enhanced Photodynamic Therapy Treatment of Tumor. *Nat. Commun.* **2020**, *11*, 357.

(35) Zhou, J.; Li, M.; Hou, Y.; Luo, Z.; Chen, Q.; Cao, H.; Huo, R.; Xue, C.; Sutrisno, L.; Hao, L.; Cao, Y.; Ran, H.; Lu, L.; Li, K.; Cai, K. Engineering of a Nanosized Biocatalyst for Combined Tumor Starvation and Low-Temperature Photothermal Therapy. *ACS Nano* **2018**, *12*, 2858-2872.

(36) Wang, D.; Zhou, J.; Chen, R.; Shi, R.; Wang, C.; Lu, J.; Zhao, G.; Xia, G.; Zhou, S.; Liu, Z.; Wang, H.; Guo, Z.; Chen, Q. Core-Shell Metal-Organic Frameworks as Fe<sup>2+</sup> Suppliers for Fe<sup>2+</sup>-Mediated Cancer Therapy under Multimodality Imaging. *Chem. Mater.* **2017**, *29*, 3477-3489.

(37) Hu, M.; Torad, N. L.; Yamauchi, Y. Preparation of Various Prussian Blue Analogue Hollow Nanocubes with Single Crystalline Shells. *Eur. J. Inorg. Chem.* **2012**, 4795-4799.

(38) Sullivan, S. P.; Koutsonanos, D. G.; Del Pilar Martin, M.; Lee, J. W.; Zarnitsyn, V.; Choi, S. O.; Murthy, N.; Compans, R. W.; Skountzou, I.; Prausnitz, M. R. Dissolving Polymer Microneedle Patches for Influenza Vaccination. *Nat. Med.* **2010**, *16*, 915-920.

(39) Kaneda, Y.; Tsutsumi, Y.; Yoshioka, Y.; Kamada, H.; Yamamoto, Y.; Kodaira, H.; Tsunoda, S.; Okamoto, T.; Mukai, Y.; Shibata, H.; Nakagawa, S.; Mayumi, T. The Use of PVP as a Polymeric Carrier to Improve the Plasma Half-Life of Drugs. *Biomaterials* **2004**, *25*, 3259-3266.

(40) Ishihara, T.; Maeda, T.; Sakamoto, H.; Takasaki, N.; Shigyo, M.; Ishida, T.; Kiwada, H.; Mizushima, Y.; Mizushima, T. Evasion of the Accelerated Blood Clearance Phenomenon by Coating of Nanoparticles with Various Hydrophilic Polymers. *Biomacromolecules* **2010**, *11*, 2700-2706.

(41) Cai, X.; Gao, W.; Ma, M.; Wu, M.; Zhang, L.; Zheng, Y.; Chen, H.; Shi, J. A Prussian Blue-Based Core-Shell Hollow-Structured Mesoporous Nanoparticle as a Smart Theranostic Agent with Ultrahigh pH-Responsive Longitudinal Relaxivity. *Adv. Mater.* **2015**, *27*, 6382-6389.

(42) Deng, G.; Zhong, L.; Sun, Y.; Liu, Z.; Wang, Q.; Gao, D.; Zhang, G.; Xu, Y. Synthesis and Magnetic Behavior of Prussian Blue Analogues Mn<sub>3</sub>[Fe(CN)<sub>6</sub>]<sub>2</sub>·12H<sub>2</sub>O Porous Nanoparticles. *J. Solid State Chem.* **2018**, *268*, 175-181.

(43) Gerweck, L. E.; Seetharaman, K. Cellular pH Gradient in Tumor *versus* Normal Tissue: Potential Exploitation for the Treatment of Cancer. *Cancer Res.* **1996**, *56*, 1194-1198.

(44) Pogue, B. W.; O'Hara, J. A.; Demidenko, E.; Wilmot, C. M.; Goodwin, I. A.; Chen, B.; Swartz, H. M.; Hasan, T. Photodynamic Therapy with Verteporfin in the Radiation-Induced Fibrosarcoma-1 Tumor Causes Enhanced Radiation Sensitivity. *Cancer Res.* **2003**, *63*, 1025-

33.

(45) Blanco, E.; Shen, H.; Ferrari, M. Principles of Nanoparticle Design for Overcoming Biological Barriers to Drug Delivery. *Nat. Biotechnol.* **2015**, *33*, 941-951.

(46) Dai, Y.; Xu, C.; Sun, X.; Chen, X. Nanoparticle Design Strategies for Enhanced Anticancer Therapy by Exploiting the Tumour Microenvironment. *Chem. Soc. Rev.* **2017**, *46*, 3830-3852.

(47) Wan, S. S.; Cheng, Q.; Zeng, X.; Zhang, X. Z. A Mn(III)-Sealed Metal-Organic Framework Nanosystem for Redox-Unlocked Tumor Theranostics. *ACS Nano* **2019**, *13*, 6561-6571.

(48) Cai, X.; Xie, Z.; Ding, B.; Shao, S.; Liang, S.; Pang, M.; Lin, J. Monodispersed Copper(I)-Based Nano Metal-Organic Framework as a Biodegradable Drug Carrier with Enhanced Photodynamic Therapy Efficacy. *Adv. Sci.* **2019**, *6*, 1900848.

(49) Dong, Z.; Feng, L.; Hao, Y.; Li, Q.; Chen, M.; Yang, Z.; Zhao, H.; Liu, Z. Synthesis of CaCO<sub>3</sub>-Based Nanomedicine for Enhanced Sonodynamic Therapy *via* Amplification of Tumor Oxidative Stress. *Chem* **2020**, *6*, 1391-1407.

(50) Revesz, L.; Edgren, M. R.; Wainson, A. A. Selective Toxicity of Buthionine Sulfoximine (BSO) to Melanoma Cells *in Vitro* and *in Vivo*. *Int. J. Radiat. Oncol. Biol. Phys.* **1994**, *29*, 403-406.

(51) Allen, T. M.; Cullis, P. R. Drug Delivery Systems: Entering the Mainstream. *Science* **2004**, *303*, 1818-1822.

(52) Phua, S. Z. F.; Yang, G.; Lim, W. Q.; Verma, A.; Chen, H.; Thanabalu, T.; Zhao, Y. Catalase-Integrated Hyaluronic Acid as Nanocarriers for Enhanced Photodynamic Therapy in Solid Tumor. *ACS Nano* **2019**, *13*, 4742-4751.

(53) Hifumi, H.; Yamaoka, S.; Tanimoto, A.; Citterio, D.; Suzuki, K. Gadolinium-Based Hybrid Nanoparticles as a Positive MR Contrast Agent. *J. Am. Chem. Soc.* **2006**, *128*, 15090-15091.

(54) Cai, X.; Jia, X.; Gao, W.; Zhang, K.; Ma, M.; Wang, S.; Zheng, Y.; Shi, J.; Chen, H. A Versatile Nanotheranostic Agent for Efficient Dual-Mode Imaging Guided Synergistic Chemo-Thermal Tumor Therapy. *Adv. Funct. Mater.* **2015**, *25*, 2520-2529.

(55) Liu, J.; Yang, Y.; Zhu, W.; Yi, X.; Dong, Z.; Xu, X.; Chen, M.; Yang, K.; Lu, G.; Jiang, L.; Liu, Z. Nanoscale Metal-Organic Frameworks for Combined Photodynamic & Radiation Therapy in Cancer Treatment. *Biomaterials* **2016**, *97*, 1-9.

